Insight on MWW siliceous zeolites: From 2D precursors toward 3D structure

Francesca Rosso [a], Alessia Airi [a,1], Matteo Signorile [a], Eddy Dib [b,**], Silvia Bordiga [a], Valentina Crocellà [a], Svetlana Mintova [b], Francesca Bonino [a,*]

[a] Department of Chemistry, NIS and INSTM Reference Centre, Università di Torino, Via G. Quarello 15, 10135 and Via P. Giuria 7, 10125, Torino, Italy
[b] Normandie Univ, ENSICAEN, UNICAEN, CNRS, Laboratorie Catalyse et Spectrochimie, 14000, Caen, France

ARTICLE INFO

ABSTRACT

ITQ-1 layered zeolites, with MWW framework, were prepared using different synthesis and calcination procedures and fully characterized by means of X-ray diffraction, scanning electron microscopy, N_2 sorption and vibrational and nuclear magnetic resonance spectroscopies. Exploring different compositions of the precursor gel, the role of the Organic Structure Directing Agent (OSDA) was definitely disclosed. We proved that the concentration of OSDA in the synthesis gel affects the short-range crystalline order of zeolite crystals. In particular, diluted precursor gels led to the formation of low-density materials in the form of hollow spheres, with partially disordered layers, thinner crystals and high defectivity. In general, all ITQ-1 samples had the same crystalline structure but different morphology, either rose-like or hollow spheres. Moreover, the calcination procedure had an impact on the structural defects of the ITQ-1 zeolite: the higher the removal rate of the OSDA, the higher the defectivity degree of the zeolite.

1. Introduction

In the group of nanostructured materials, layered zeolites offer the possibility to combine the high reactivity and thermal stability of zeolites catalysts with the versatility of layered solids [1–3]. Among the known layered zeolites, those with FER [4], MWW [5] and MFI [6,7] framework types are notable. The MCM-22 [8–10] (aluminosilicate with MWW [5] topology) is used for the industrial production of ethylbenzene [1,11,12]. The MWW framework features two independent pore systems. The first is composed by 10 Member-Ring (MR) sinusoidal channels (ø ≈ 5.2 Å), running intralayer, whereas the second is composed of internal super-cages with a dimension of 7.1 Å × 18.2 Å, connected to each other by the 10 MR apertures. The MWW zeolites are distinguished by different connection modes between the layers and the connections vary depending on the synthesis procedure. MCM-22(P), the parent of the MCM-22 material [10], is composed of MWW single layers, stacked by the means of hydrogen bonds and dispersion forces [13] with the Organic Structure Directing Agent (OSDA) i.e. hexamethyleneimine (HMI) [8,9]. Upon calcination, the layers condense to form the MCM-22 zeolite [8,14]. If the hydrogen bonds system of MCM-22(P) is swollen, the material can be pillared to form a hierarchical analogue

named MCM-36 [15]. Alternatively, the swollen precursor can be delaminated, to form a material with separated single layers named ITQ-2 [16]. By varying the composition of the synthesis gel is it also possible to synthesize a precursor where the single layers are already condensed before the calcination (MCM-49) [17] or scattered from MCM-22(P) (MCM-56) [18–20]. An interesting interpretation of the condensation phenomenon yielding MCM-22 or MCM-56 from MCM-22 (P) predicts that this is governed by the balance between dispersions forces and hydrogen bonds between layers and OSDA molecules [13].

When layered precursors are involved, the 10 MR channels are formed during the hydrothermal crystallization of the zeolite in the presence of the OSDA and the interlayer super-cages are formed throughout the calcination procedure, i.e. during the removal of the OSDA.

For the siliceous analogue, i.e. ITQ-1, the transition between all possible structures is still blurred. This zeolite is promising in catalysis, both as support for active phases nanoparticles or for the insertion of heteroatoms in the framework [21–24]. In this context, a comprehensive study of ITQ-1 combining both structural and morphological aspects is necessary to understand the effects of the synthesis parameters. The synthesis of ITQ-1 is reported to occur with the N,N,

Table 1
ITQ-1 samples synthesized from different precursor gels, exploiting different calcination procedures.

Sample	Gel molar composition	Calcination procedure
rose-ITQ-1-HS	1 SiO$_2$: 0.2 TMAdaOH : 0.3 HMI : 0.07 K$_2$O : 0.07 CO$_3^{2-}$: 30 H$_2$O	none
rose-ITQ-1-calcA	1 SiO$_2$: 0.2 TMAdaOH : 0.3 HMI : 0.07 K$_2$O : 0.07 CO$_3^{2-}$: 30 H$_2$O	A
rose-ITQ-1-calcB	1 SiO$_2$: 0.2 TMAdaOH : 0.3 HMI : 0.07 K$_2$O : 0.07 CO$_3^{2-}$: 30 H$_2$O	B
sf-ITQ-1-HS	1 SiO$_2$: 0.25 TMAdaOH : 0.31 HMI : 44 H$_2$O	none
sf-ITQ-1-calcA	1 SiO$_2$: 0.25 TMAdaOH : 0.31 HMI : 44 H$_2$O	A
sf-ITQ-1-calcB	1 SiO$_2$: 0.25 TMAdaOH : 0.31 HMI : 44 H$_2$O	B

N-trimethyl-adamantil-ammonium hydroxide (TMAdaOH) as OSDA, but the concurrent use of HMI is necessary for a reproducible procedure [22, 25].

In this work, two different compositions of the precursor synthesis gel were chosen as starting point. They differ in water (H$_2$O) content, ratio between the OSDAs, OH and Si and the presence of alkali cations. Particular attention was paid to the as-synthesized ITQ-1 material to understand the role of OSDAs either during the hydrothermal synthesis or during the calcination. In particular, the role of OSDAs during the synthesis and calcination procedures was disclosed using a combination of spectroscopic, thermogravimetric and elemental analyses on both the organic and inorganic fractions of the materials. The differences in the morphological and structural properties of the ITQ-1 samples were carefully determined by means of diffraction methods, electron microscopy and spectroscopic techniques and the origin of the differences was found to be the amount and location of OSDAs and H$_2$O molecules in the as-synthesized material.

2. Experimental

2.1. Materials

For the ITQ-1 samples synthesis, Aerosil® 200 (from Evonik Industries), TMAdaOH (25 wt% in water, from TCI), HMI (99 % from Sigma Aldrich), potassium carbonate (K$_2$CO$_3$, anhydrous, ACS reagent, from Sigma Aldrich) and Milli-Q water (18.2 MΩ cm) were used. All the reagents were used as received without further purification.

2.2. Synthesis of the ITQ-1 samples

Two sets of ITQ-1 samples using different gels were hydrothermally synthesized. The molar composition of the first gel was 1 SiO$_2$: 0.2 TMAdaOH : 0.3 HMI : 0.07 K$_2$O : 0.07 CO$_3^{2-}$: 30 H$_2$O [22]. In a typical procedure, 8.45 g of TMAdaOH solution, 1.49 g of HMI and 0.4837 g of K$_2$CO$_3$ were added to 20.68 g of Milli-Q water in this order. The solution was stirred at room temperature for 30 min to allow complete dissolution of K$_2$CO$_3$ and then 3.004 g of Aerosil® 200 were gradually added under vigorous stirring, until a homogeneous gel was obtained. The molar composition of the second gel was 1 SiO$_2$: 0.25 TMAdaOH : 0.31 HMI : 44 H$_2$O [25]. In a typical procedure, 7.29 g of TMAdaOH solution and 1.06 g of HMI were added to 21.89 g of Milli-Q water. Thus, 2.0728 g of SiO$_2$ were gradually added to the above solution under vigorous stirring, until a homogeneous gel was obtained.

Each gel (approximately 30 ml each) was transferred into a 45 ml Telfon lined stainless steel digestor and heated at 150 °C for 5 days under tumbling conditions, at 60 rpm. After the hydrothermal crystallization, the samples were recovered by filtration, washed with deionized water until a pH < 8 was reached and dried at room temperature. Two as-synthesized samples obtained from gels with different molar compositions are called rose-ITQ-1-HS and sf-ITQ-1-HS respectively. A portion of each as-synthesized sample was calcined in a tubular oven with two different procedures: *procedure A* consists in the heating of the sample with a rate of 1 °C/min till 550 °C under flow of dry air, followed by 7 h heating under the same flow; *procedure B* consists in heating the

sample with a ramp of 1 °C/min till 580 °C, under a flow of N$_2$, followed by 3 h heating under a flow of O$_2$. The temperatures (580 or 550 °C) and the length (7 or 3 h) of the isotherms, coupled with each atmosphere were chosen to obtain samples with more divergent properties, based on preliminary results (not shown for the sake of brevity). Thus, the calcined zeolite samples are called rose-ITQ-1-calcA, rose-ITQ-1-calcB, sf-ITQ-1-calcA and sf-ITQ-1-calcB. The synthesis conditions and the sample names are summarized in Table 1.

2.3. Characterization of ITQ-1 samples

X-Rays Diffraction (XRD) patterns were collected on the as-synthesized and calcined samples with a Cu K$_\alpha$ radiation, on a PAN-analytical X'Pert diffractometer (Bragg-Brentano geometry), equipped with a X'celerator strip detector, in the range 5° ≤ 2θ ≤ 50°, with a step of 0.02° and 50 s/° of integration. Cu K$_\beta$ was suppressed with a Ni filter.

Scanning Electron Microscopy (SEM) images of the as-synthesized and calcined samples were obtained using a Mira\\Tescan microscope. The images were collected on the metal sputtered samples (70:30 Pt:Pd film of thickness of 2 nm). The distribution of zeolite particles with different thicknesses (particles dimension along the *c* axis) was measured based on at least 175 particles per samples.

N$_2$ physisorption isotherms of the calcined samples were recorded on a Micromeritics 3Flex instrument at −196 °C. Prior to the measurement, the powders were outgassed overnight at 120 °C and at least 7 h at 400 °C. The Specific Surface Areas (SSAs) were determined with both the Brunauer-Emmett-Teller (BET) and Langmuir models. The models were applied in pressure ranges suitable for obtaining a monolayer capacity included in the selected p/p^0 (for the BET) or p (for the Langmuir) linearization range [26]. The cumulative pore volume and the pore size distribution were obtained by applying the Non-Local Density Functional Theory (NL-DFT); the pores were modelled as slit pores, using the "N$_2$@ 77-Carbon, original DFT" available in the Microactive software [27]. The model was applied in the whole range of p/p^0 with a regularization of 10^{-3}.

The infrared (IR) spectra of the calcined samples were recorded both in transmission and in Attenuated Total Reflectance (ATR) mode. The transmission IR spectra were collected with a Bruker Vertex 70 spectrophotometer, equipped with a Mercury Cadmium Telluride (MCT) cryo-detector on a self-supporting pellet of the pure sample, placed inside a quartz cell with KBr windows. The pellet was mechanically protected by a gold envelope and treated prior to the acquisition to remove the physisorbed molecules and possible organic pollutants. The treatment provides a 5 °C/min ramp to 500 °C followed by 30 min in isothermal conditions at 500 °C while outgassing. Then, 100 mbar of pure O$_2$ were dosed in the cell while at 500 °C and left in contact with the sample for 30 min to oxidize organic residues. The sample was then outgassed at 500 °C until the final pressure was $<10^{-3}$ mbar. The spectrum was acquired under vacuum at *ca.* 40 °C (the temperature reached by the sample under the IR beam), by accumulating 32 scans (64 for the background) at 2 cm^{-1} of resolution. The spectra intensity was internally normalized to the overtones bands of bulk vibration modes (bands peaked at 1990, 1877 and 1665 cm^{-1}). The ATR-IR spectra were collected on the powdered sample without pre-treatment

accumulating 64 scans (128 for the background) at 2 cm^{-1} of resolution on a Bruker Vertex 70 spectrophotometer equipped with a Deuterated TriGlycine Sulfate (DTGS) detector and an ATR Platinum accessory, equipped with a single reflection diamond internal reflection element. The spectra were internally normalized in intensity using the symmetric Si–O–Si stretching band, centered at 800 cm^{-1}.

The Raman spectra of the calcined samples were measured in air without pre-treatment using the 244 nm excitation line (Coherent MotoFred 300C, frequency doubled Ar$^+$ laser) on a Renishaw inVia Raman microscope spectrometer, equipped with 3600 line/mm grating and UV-enhanced Charge-Coupled Device (CCD) detector. The laser was focused on the sample through a 15x objective.

One Pulse (OP) ^{29}Si and Cross Polarization (CP) ^{29}Si{^{1}H} Magic-Angle Spinning (MAS) Nuclear Magnetic Resonance (NMR) spectra were acquired at 79.4 MHz on a Bruker Avance III-HD 400 (9.4 T), using 4.0-mm outer diameter probe. For OP, a radiofrequency of 30 kHz and a recycle delay of 15 s was used. A recycle delay of 5 s and a contact time of 5 ms were used for ^{29}Si CP-MAS experiments. For ^{29}Si OP- and CP-MAS experiments 4096 and 2048 transients were acquired respectively. The ^{29}Si OP-MAS spectra of the calcined rose-ITQ-1-calcA and rose-ITQ-1-calcB and of the as-synthesized rose-ITQ-1-HS samples were deconvoluted with Lorentzian peaks, using the program Fityk. For the calcined samples, the deconvoluted peaks were added at chemical shift values that were kept coherent with theoretical chemical shifts computed with the following equation (eq. (1)) [28].

$$\delta_{iso} = 11.531\langle r_{SiO}\rangle + 27.280\sigma(r_{SiO}) + 83.7430\cos(\langle\theta_{SiOSi}\rangle) + 0.20246\sigma(\theta_{SiOSi}) - 59.999 \qquad (1)$$

Where δ_{iso} is the chemical shift (ppm), $\langle r_{SiO}\rangle$ is the average Si–O distance, $\sigma(r_{SiO})$ is its standard deviation, $\langle\theta_{SiOSi}\rangle$ is the average Si–O–Si angle and $\sigma(\theta_{SiOSi})$ is its standard deviation. The Si–O–Si angles and the Si–O distances were obtained from the cif file for the MWW framework, downloaded from the Database of Zeolite Structures present on the website of the International Zeolite Association (IZA) [29], without further refinement.

^{13}C OP-MAS-NMR spectra of the as-synthesized rose-ITQ-1-HS and sf-ITQ-1-HS samples were acquired at 100.6 MHz on a Bruker Avance III-HD 400 (9.4 T), using 4.0-mm outer diameter probe. Radiofrequency pulses of 38.5 kHz and a recycle delay of 2 s were used. For each spectrum, 6000 transients were acquired.

The elemental analysis of the as-synthesized samples was performed using a Thermo Nicolet FlashEA 1112 Series CHNS analyzer; the measurement was repeated three times for each as-synthesized sample and the results were averaged.

The Thermogravimetric (TG) analyses of the as-synthesized samples were performed with a SDT Q600 analyzer by TA instrument, placing approximately 6 mg of sample inside the alumina pan. Each as-synthesized sample was analyzed with the following two procedures. *Procedure A:* heating ramp of 1 °C/min to 550 °C under dry air flow, followed by heating for 3 h under the same flow. *Procedure B:* heating ramp of 1 °C/min to 580 °C under N$_2$ flow, followed by a 3 h heating under dry air flow. The flow was set to 100 ml/min and the isotherm of *procedure A* was limited to 3 h because the plateau was already achieved.

The calcination procedure of the samples was followed by transmission IR; a self-supporting pellet of pure as-synthesized samples, mechanically protected by a gold envelope was used. The pellet was placed inside the heating element of an AABSPEC CXX cell, equipped with two thermocouples to control the temperature of the sample and to work under gas flow. Each as-synthesized sample was measured with the following experimental procedures. *Procedure A*: 30 min under flow at 30 °C for the sake of equilibration, heating ramp of 1 °C/min to 550 °C

under a flow of 20 vol% O$_2$ in Ar, followed by 3 h heating under the same flow. *Procedure B*: 30 min under flow at 30 °C for the sake of equilibration, heating ramp of 1 °C/min to 550 °C under a flow of pure Ar, followed by 3 h heating under a flow of 20 vol% O$_2$ in Ar. Ar was used as inert gas instead of N$_2$ for the mass analysis. The spectra of the pelletized sample during the heating were collected each 4 min accumulating 32 scans, with a resolution of 4 cm^{-1}, on a Thermo Scientific Nicolet iS50 FTIR spectrometer, equipped with an MCT detector. The gas phase downstream to the cell was analyzed by mass spectrometry (Quadrupole Pfeiffer Omnistar GSD 301).

3. Results and discussion

3.1. Characterization of crystalline structure and morphology of ITQ-1 samples

Fig. 1 shows the XRD patterns of the as-synthesized rose-ITQ-1-HS and sf-ITQ-1-HS samples (a) and of the calcined rose-ITQ-1-calcA, rose-ITQ-1-calcB (b), sf-ITQ-1-calcA and sf-ITQ-1-calcB (c) samples in the 5°–50° 2θ range. The XRD patterns of the samples reveal the MWW topology, and the positions and bandwidth of the reflections are consistent with what reported in the literature [22,25,30]. A pronounced difference between the as-synthesized and the corresponding calcined patterns can be noted. It testifies a significant structural change that induces variation of specific reflections. The Bragg peaks with Miller indexes *hk*0 (e.g. 100, 200, 220 and 310, corresponding to directions parallel to the *ab* plane) do not move upon calcination, while those with Miller indexes *hkl* with *l*≠0 (e.g. 002, 101 and 102, directions that have a component perpendicular to the *ab* plane) shift to high 2θ angles [9,30] (Fig. S1). This indicates that the as-synthesized rose-ITQ-1-HS and sf-ITQ-1-HS samples are formed of separated single layers, as MCM-22(P), that condense upon calcination, causing the contraction of the unit cell along the *c* direction, as already reported [22,25,30].

Both the as-synthesized and calcined samples display sharp and broad reflections. The sharp ones have Miller indexes *hk*0, suggesting a pronounced preferential growth of the crystal parallel to the *ab* plane. Moreover, among the broad peaks (having Miller indexes *hkl* with *l*≠0), those in the XRD patters of samples sf-ITQ-1-HS, -calcA and -calcB are even broader and less resolved than their analogue in samples rose-ITQ-1-HS, -calcA and -calcB. This indicates that the broadening occurs along the *c* direction. It could be a lower degree of order or a lower crystal dimension along the *c* axis in sample sf-ITQ-1 compared to sample rose-ITQ-1.

To clarify this point, SEM images were recorded at different magnifications (Fig. 2 and Figs. S2–S7). No relevant difference in morphology is observed comparing each as-synthesized sample (rose-ITQ-1-HS and sf-ITQ-1-HS) with the corresponding calcined ones, so the calcination procedure does not seem to affect the morphology. Modifications in the aggregation way are instead observed by comparing samples obtained with different molar composition of the synthesis gel (namely rose-ITQ-1-HS, -calcA or -calcB on one hand and sf-ITQ-1-HS, -calcA or -calcB on the other). The low magnification images of the rose-ITQ-1 show rose-like small agglomerates of uniform size and shape (Fig. 2a,e,i), while sf-ITQ-1 samples form hollow macro-sized sphere aggregates (Fig. 2c,g,k). The properties of the hollow spheres (sf-ITQ-1) were investigated: the average particle diameter (Table 2) and the corresponding size distribution (Fig. S9) were measured. The size distribution is very similar among the as-synthesized and the calcined samples and it is not affected by the calcination procedure. The
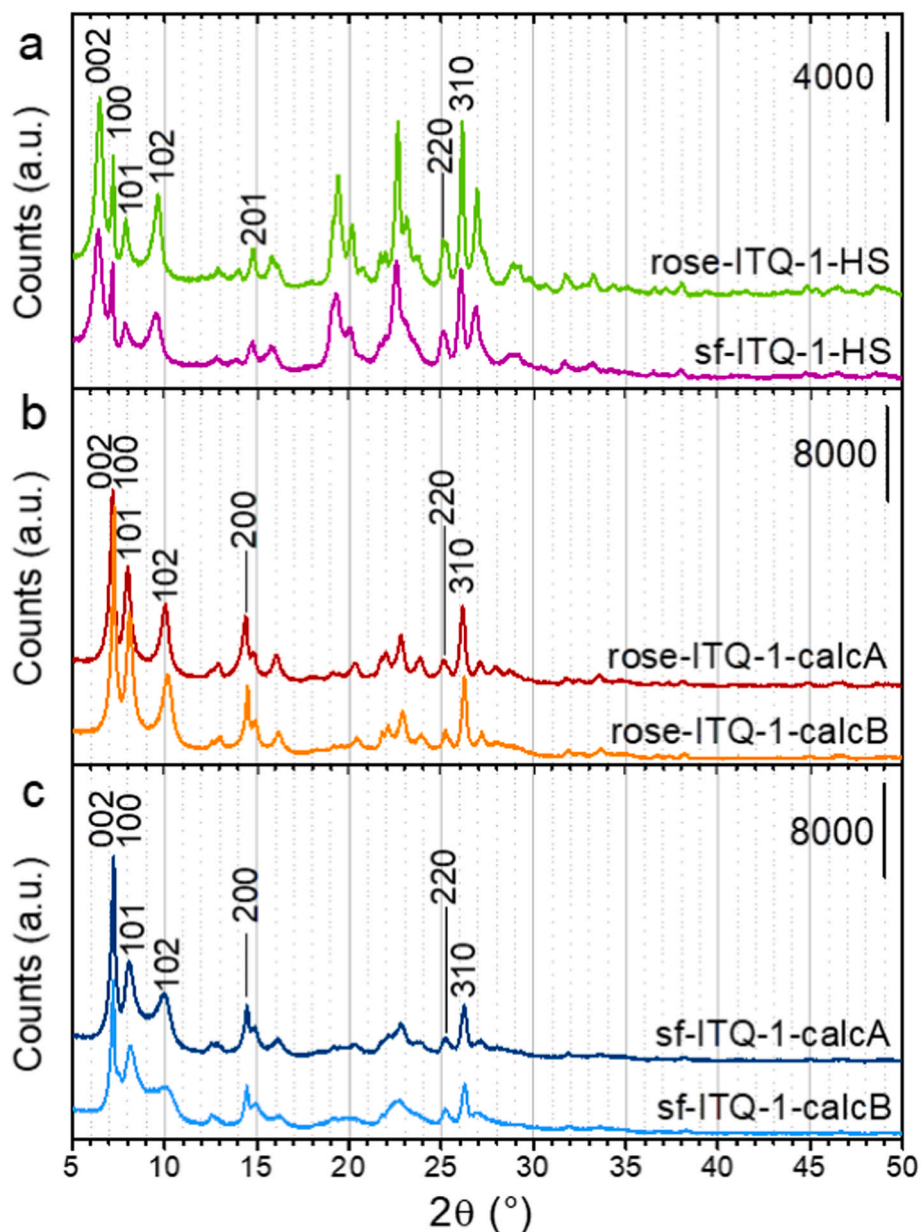
Fig. 1. XRD patterns of the as-synthesized rose-ITQ-1-HS and sf-ITQ-1-HS samples (a), calcined rose-ITQ-1-calcA and rose-ITQ-1-calcB (b), and calcined sf-ITQ-1-calcA and sf-ITQ-1calcB (c) samples.

aggregation in zeolites with MWW framework was already reported in the literature, but it was obtained by employing a carbon black [31] or BP 2000 [32] as hard templates or di-quaternary ammonium surfactants [33] as soft templates in the case of MCM-22. In our study, it is possible that higher TMAdaOH/SiO$_2$ and HMI/SiO$_2$ ratios in the precursor synthesis gel used for preparation of sample sf-ITQ-1-HS give rise to the formation of aggregated hollow macro-sized spheres. In contrast, rose-like small aggregates are obtained at lower TMAdaOH/SiO$_2$ and HMI/SiO$_2$ ratios. Further studies are needed to clarify the effect of OSDAs on the macro-sphere formation.

Regardless of how they are assembled, the primary particles of ITQ-1 are nanosheets of nearly hexagonal morphology, as shown in Fig. 2b,d,f, h,j,l. The average nanosheet thickness (Table 2) and the corresponding thickness size distribution (Table S1 and Fig. S8) were measured. The sf-ITQ-1-HS, -calcA and -calcB samples have slightly thinner particles than the rose-ITQ-1-HS, -calcA and -calcB. The thickness size distribution plots are quite superimposed, but the maximum of each distribution is clearly distinguishable and different for each sample. The variation of

the nanosheet thickness can be related to the differences in peaks broadening observed in the XRD patterns, by applying the following assumptions: (1) the size of the crystallite domain could be compared to the size of the hexagonal nanosheets visible in the SEM images and (2) the broadening of the XRD peaks is the manifestation of the average crystallite dimension, mediated on the bulk of the material (represented by the slight shift of the thickness size distribution). Accordingly, the sf-ITQ-1-HS, -calcA and -calcB samples, that display a greater peak broadening along *c* axis, are composed of thinner particles compared to rose-ITQ-1-HS, -calcA or -calcB. Furthermore, the lower particle thickness causes a lower coherence in diffraction along *c* axis. If the layers stack in an uneven way during the hydrothermal treatment, the crystal growth would probably be more frequently interrupted and the crystals would be thinner. We observe that the layer stack in the rose-ITQ-1 sample occurs in a more aligned way, resulting in crystals growth along the *c* axis (sharper Bragg reflections), while, in the sf-ITQ-1 samples, a slight mismatch between the layers hinders the growth along *c* axis and thinner nanosheets are formed. The thickness size distribution
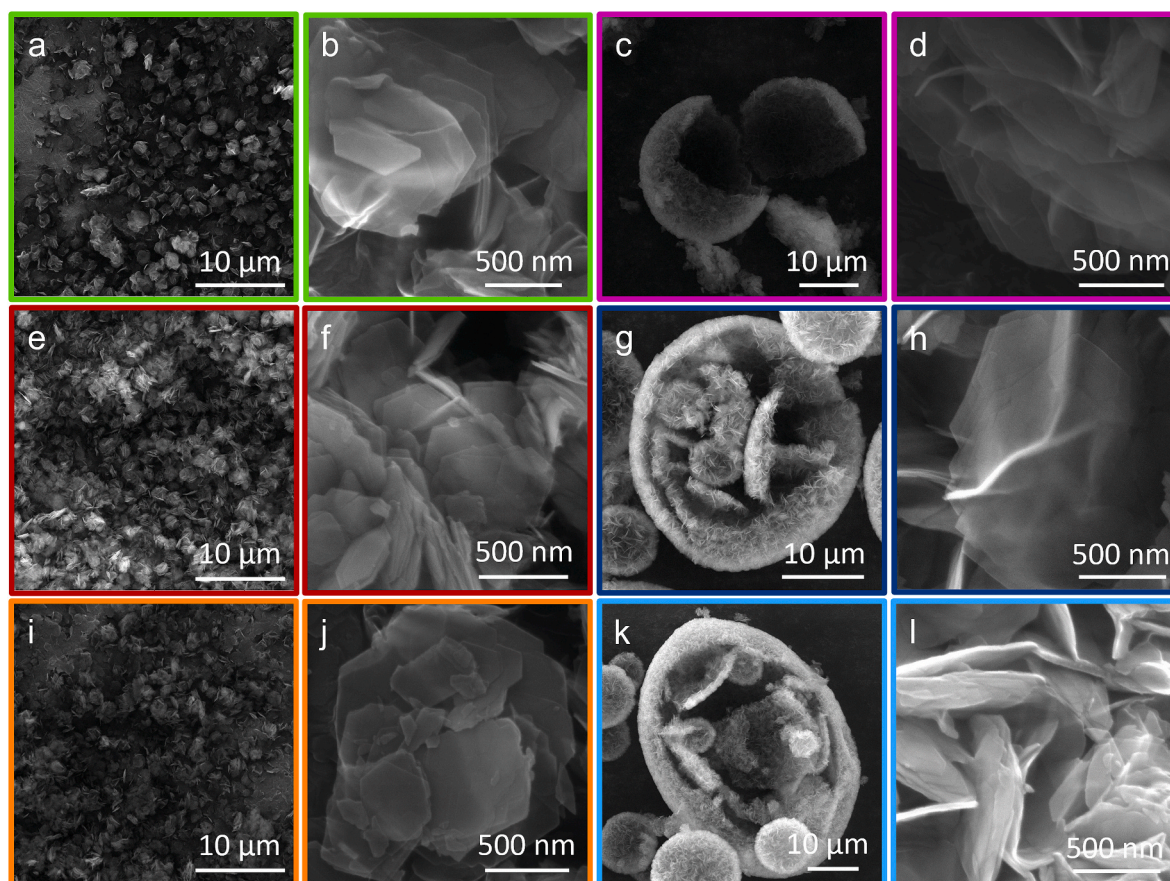
Fig. 2. SEM images at different magnifications of samples rose-ITQ-1-HS (a, b - green), sf-ITQ-1-HS (c, d - purple), rose-ITQ-1-calcA (e, f - red), sf-ITQ-1-calcA (g, h - blue), rose-ITQ-1-calcB (i, j - orange) and sf-ITQ-1-calcB (k, l – light blue). For each sample, the image on the left is at high magnification and the image on the right is at low magnification.

Table 2
Average nanosheets thickness (particle dimension along the *c* axis) of all the samples and sphere diameters of sf-ITQ-1 samples.

Sample	Particle thickness (nm)	Spheres diameter (μm)
rose-ITQ-1-HS	21 ± 1	–
rose-ITQ-1-calcA	23 ± 1	–
rose-ITQ-1-calcB	18 ± 1	–
sf-ITQ-1-HS	14 ± 2	14 ± 1
sf-ITQ-1-calcA	14 ± 1	13 ± 1
sf-ITQ-1-calcB	13 ± 1	11 ± 1

is also moderately affected by the calcination procedure, since the rose-ITQ-1-calcA and sf-ITQ-1-calcA samples are slightly thicker than their analogues rose-ITQ-1-calcB and sf-ITQ-1-calcB, respectively.

The textural properties of all the calcined samples were studied by N_2 physisorption at -196 °C. The N_2 physisorption isotherms plotted in linear (a) and logarithmic (b) scale are reported in Fig. 3. All isotherms are of type I, typical of microporous materials, with a H3 hysteresis loop at high relative pressure values (arising from the filling of interparticle voids between plate-like particles) [26]. The SSAs obtained with the BET and Langmuir models and the micropore volume (Table 3, S2, S3 and Figs. S10–S12) are coherent with the zeolitic framework type [5]. The samples calcined with *procedure B* exhibit a significantly lower micropore volume and SSAs values than those calcined with *procedure A* (Fig. 3c), probably due to a partial occlusion of the pores during the heating ramp under inert flow. This is particularly evident for sf-ITQ-1-calcB. Moreover, sf-ITQ-1 samples show an additional family of voids in the micropore range (10–20 Å), not related with the crystalline framework structure. This could be ascribed to random voids located in

the interlayer space as a consequence of the mismatch in the layers stacking.

3.2. Spectroscopic characterization of ITQ-1 samples

The differences between the ITQ-1 samples at an atomic scale were revealed by an IR spectroscopic study. The low frequency region of ATR-IR and Raman spectra of the ITQ-1 samples are depicted in Fig. 4a and b. The vibrations are collective bending modes of groups of atoms that have specific positions. Information about the structural order can be obtained from the broadening of the bands [19,34,35]. In the ATR-IR spectra of zeolites with MWW topology, bands assigned to the stretching of double-6-ring (D6R) [36–38] units are present. They are centered at 611 and 562 cm^{-1} in the ATR-IR spectra of all the samples, but appear broader and less intense in the sf-ITQ-1 than in rose-ITQ-1 samples, probably due to their higher defectivity. This is in line with what observed by XRD. The low frequency region of the Raman spectra (Fig. 4b) provides similar information. Bands assigned to collective vibrations of rings composed of different number of tetrahedra are present [39,40]. In our spectra, a group of bands at 522, 483 and 345 cm^{-1} could be assigned to the bending vibrations of 4-, 5- and 6-member ring groups in the MWW framework, respectively [39]. The above mentioned bands have a lower intensity for sf-ITQ-1-calcA and sf-ITQ-1-calcB samples compared to rose-ITQ-1-calcA and rose-ITQ-1-calcB. This further confirms the higher defectivity of sf-ITQ-1 samples.

In the higher frequency region of the ATR-IR spectra (Fig. 4a), a broad band at 960 cm^{-1} covering almost the whole transparency window between the asymmetric (1300-900 cm^{-1}) and symmetric (850-750 cm^{-1}) Si–O–Si stretching bands is observed [35]. The band at 960
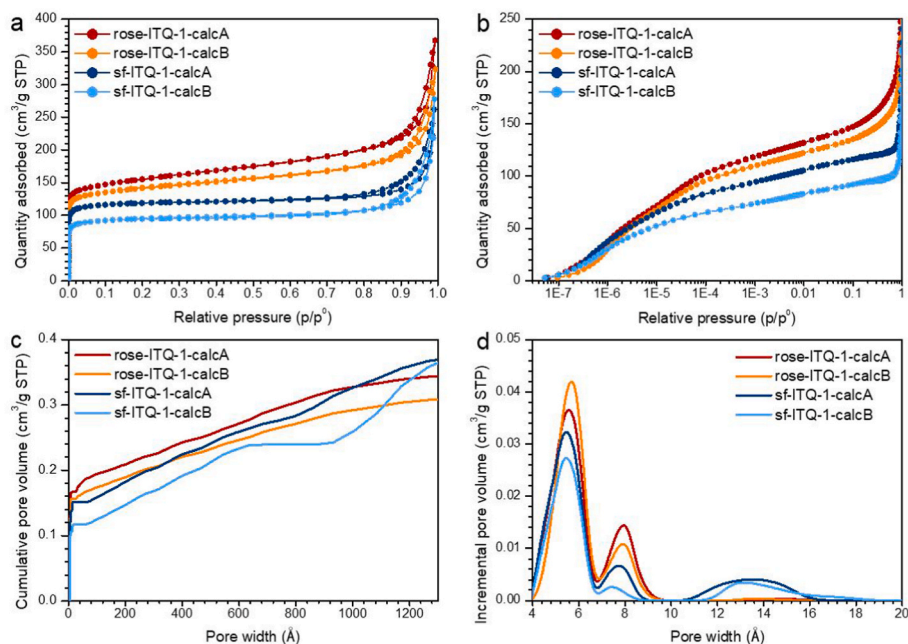
Fig. 3. Volumetric N_2 adsorption/desorption isotherms at - 196 °C in the whole relative pressure range, plotted in linear (a) and semi-logarithmic scale (b). Cumulative pore volume plot in the 0–1300 Å pore size range (c) and pore size distributions in the micropore size range (<20 Å, points connected by a B-spline function) (d), computed by NL-DFT method applied to the N_2 adsorption isotherms in the whole relative pressure range.

Table 3
SSAs calculated with the BET and Langmuir models and micropore (V_{micro}) and interparticle voids (V_{ipv}) volumes computed using the NL-DFT method.

Sample	BET SSA[a] (m^2/g)	Langmuir SSA[b] (m^2/g)	V_{micro}[c] (cm^3/g STP)	V_{ipv}[d] (cm^3/g STP)
rose-ITQ-1-calcA	586 ± 1	676 ± 5	0.17	0.03
rose-ITQ-1-calcB	538 ± 1	616 ± 4	0.16	0.03
sf-ITQ-1-calcA	465 ± 2	525 ± 1	0.15	0.03
sf-ITQ-1-calcB	368 ± 1	417 ± 2	0.12	0.03

[a] Calculated in the 0.008–0.08 p/p^0 range.
[b] Calculated in the 15–200 mbar pressure range.
[c] Calculated from the cumulative pore volume plot for pores size <20 Å
[d] Calculated from the cumulative pore volume plot by difference of the total pore volume by V_{micro}.

cm^{-1} was already observed in siliceous zeolites such as silicalite-1 and it is associated to a localized stretching mode of the $O_3Si–OH$ group [35]. The presence of silanols groups in a siliceous material constitutes an irregularity in the periodic crystalline structure and hence silanols are considered as "point defects" in the zeolite framework. When silanols are located at the crystal surface, they are generally described as isolated, while when they are associated to the vacancy of a Si atom they are described as silanol nests. Unfortunately, the localized stretching mode of the $O_3Si–OH$ group does not allow discriminating the amount or kind of hydroxyl groups. For this reason, the O–H stretching region (3800-3000 cm^{-1}) of the IR spectra recorded in transmission mode is presented in Fig. S13. Here, the higher frequency component (3745 cm^{-1}) is associated to external isolated silanols, while the presence of chains of hydrogen bonded (H-bonded) silanols is testified by a couple of signals due to the terminal OH group and to the OH involved in the H-bond chain. The vibration of the terminal OH group is centered at 3740 cm^{-1} in rose-ITQ-1 and at 3730 cm^{-1} in sf-ITQ-1 samples and the vibration of the H-bonded OH is present in the region 3650-3500 cm^{-1} as a broad shoulder. These hydroxyls are probably located in the interparticle space between adjacent nanosheets. The frequency of the band associated to the chain-terminal and H-bonded OH depends on the length of the chain: the longer the chain, the stronger the interaction and the lower the frequency of the signal observed [41–44]. At even lower

frequency, a broad band assigned to silanol nests is present. This band has a different intensity in the four samples, corresponding to a distinct amount of "point defects" in the materials, with the following order: rose-ITQ-1-calcB < rose-ITQ-1-calcA < sf-ITQ-1-calcB < sf-ITQ-1-calcA. The higher defectivity of sf-ITQ-1 samples is coherent with their lower long-range crystalline order and lower particle thickness. Additionally, a difference in the number of defective sites depending on the calcination procedure is clearly observed. The rose-ITQ-1-calcB and sf-ITQ-1-calcB samples, calcined with *procedure B,* are slightly less defective than their analogues rose-ITQ-1-calcA and sf-ITQ-1-calcA, calcined with *procedure A.*

The effect of chemical composition of the synthesis gel and the calcination procedure on the long-range crystalline order and defectivity of the samples will be explained in the following section.

Fig. 4c shows the ^{29}Si MAS-NMR spectra recorded with OP experiments of all the calcined and as-synthesized ITQ-1 samples. The as-synthesized samples show well resolved signals, independently of the composition of the synthesis gel (rose-ITQ-1-HS or sf-ITQ-1-HS). After the calcination, the resolution is preserved for the rose-ITQ-1-calcA and rose-ITQ-1-calcB samples while it is lost for the sf-ITQ-1-calcA and sf-ITQ-1-calcB samples. This is due to a higher local disorder (wider angular distribution) or to a higher amount of structural defects, which is in accordance with the higher silanols concentration (see transmission
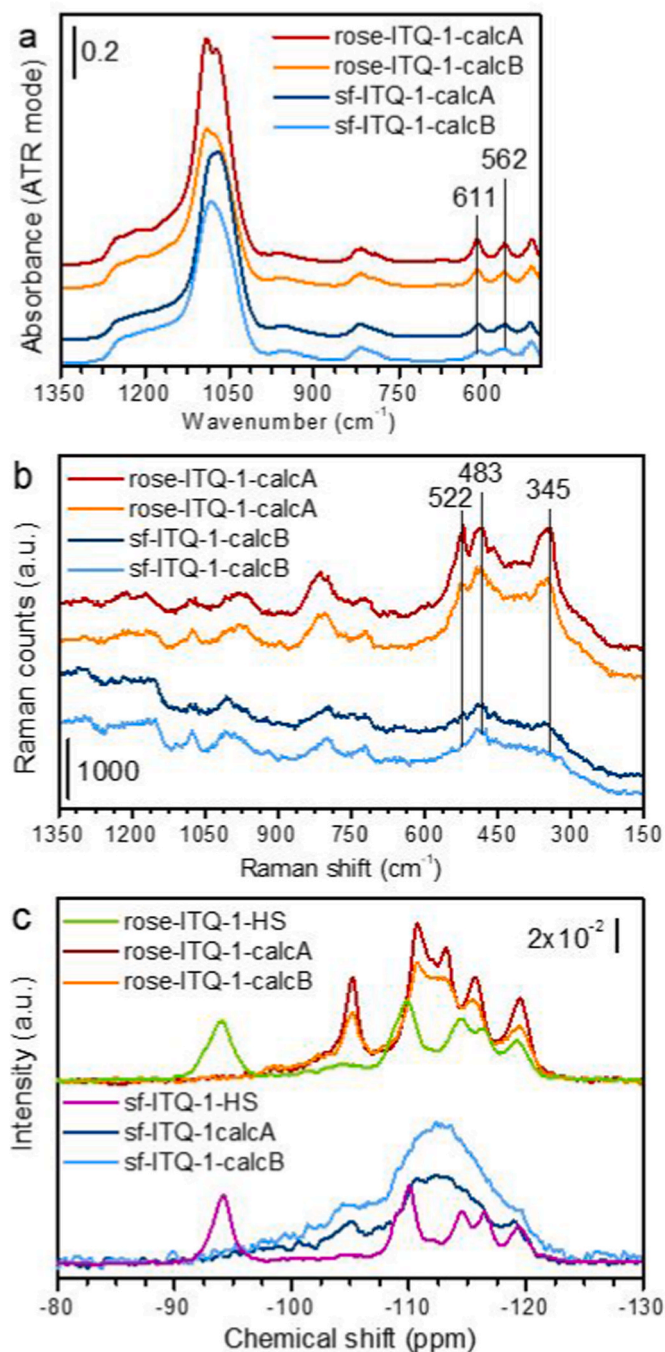
Fig. 4. ATR-IR spectra in the 1350-500 cm^{-1} range (a) and Raman spectra in the 1350-150 cm^{-1} range (b) of the calcined rose-ITQ-1-calcA, rose-ITQ-1-calcB, sf-ITQ-1-calcA, sf-ITQ-1-calcB samples, and ^{29}Si-OP-NMR spectra of the as-synthesized rose-ITQ-1-HS and sf-ITQ-1-HS and calcined rose-ITQ-1-calcA, rose-ITQ-1-calcB, sf-ITQ-1-calcA and sf-ITQ-1-calcB samples (c).

IR spectra in Fig. S13). Indeed, the ^{29}Si isotropic chemical shift observed in purely siliceous zeolites is linked to several structural parameters, among which $\langle\theta_{SiOSi}\rangle$ at each crystallographic site is the most relevant. In principle, each crystallographic site would produce a distinct signal in the ^{29}Si OP-MAS-NMR spectrum, at a distinct chemical shift value depending on $\langle\theta_{SiOSi}\rangle$. If the $\langle\theta_{SiOSi}\rangle$ distribution for a given site (namely its angular distribution) is wide, the corresponding NMR signal will broaden. Hence, the signal broadening increases together with the local disorder of the structure. Therefore, a reduced signal resolution as observed in sf-ITQ-1-calcA and sf-ITQ-1-calcB samples is an indication of the degree of local disorder.

A peculiarity is found in the spectra of the as-synthesized rose-ITQ-1-HS and sf-ITQ-1-HS samples. They show an intense signal at −94 ppm, that may correspond to a Q^3 site (tetrahedral Si site connected to three Si atoms and an atom different from Si) or to a Q^2 site (tetrahedral Si site connected to two Si atoms and two atoms different from Si). The intensity of this signal is an indication of the high amount of silanols in the as-synthesized materials and of their distinguished angular configuration. The peak at −94 ppm is relatively sharp, compared to the Q^3 site signals in the ^{29}Si CP-MAS-NMR spectra of calcined samples, obtained with a {^{1}H–^{29}Si} cross polarization (Fig. S15). This suggests that the signal at −94 ppm could be ascribed to a specific crystallographic position and that it could not be representative of a statistical distribution of silanol defective sites (as the Q^3 signals of calcined samples are). Such a big change in the ^{29}Si OP-MAS-NMR spectra before and after calcination suggests an important structural change, that occurs jointly with the layer condensation. The ^{29}Si OP-MAS-NMR spectral components of the calcined rose-ITQ-1-calcA and rose-ITQ-1-calcB samples were deconvoluted keeping the number of peaks coherent with the number of crystallographic sites of the MWW framework (eight crystallographic sites, named as reported in the Database of Zeolites Structure in the IZA website) [5]. The number of peaks used to deconvolute the spectrum of rose-ITQ-1-HS was considered the same as in the calcined samples, assuming that no modification of the hexagonal symmetry system occurs upon calcination, save the contraction of the *c* cell parameter [14,45]. This is a rough approximation, since the Si–OH groups at the surface of the single layers in rose-ITQ-1-HS, that may contribute to the signal at −94 ppm, are in principle 4 over 72 Si atoms in a unit cell (≈5 %). The relative integrated intensity of the signal at −94 ppm is too high to be exclusively due to 4 Si–OH per unit cell (vide infra), note that the structure refinement of the as-synthesized form of a zeolite with MWW framework has never been published [30]. The calculation of the initial peak positions is performed using equation (1) and the details are reported in Tables S4–S9. Fig. S15 shows the deconvoluted spectra. The relative integrated area of the spectral components of the calcined samples is consistent with the multiplicity of the crystallographic sites in the unit cell: three and five peaks show an integrated relative area coherent with a multiplicity of four and twelve respectively (Tables S7–S9). The deconvolution of the spectrum of the as-synthesized rose-ITQ-1-HS sample assuming two peaks at −94 and −93 ppm was performed. The two components are likely to be Q^3 sites [14] and hence an exceptionally high amount of Si–OH groups is present in the as-synthesized material (≈22 %), already reported in the literature [45, 46]. Despite the high amount of silanol groups, rose-ITQ-1-HS sample is crystalline, thanks to the presence of the coordinated OSDAs molecules. As previously reported, the Si–OH groups present in the as-synthesized material should condense upon calcination, by H$_2$O removal, generating the 3D zeolite [14,30,46]. The amount of Si–OH groups in the purely siliceous as-synthesized zeolite ITQ-1 is too high to be ascribed to a simple condensation of perfectly formed separated layers (as what occurs e.g. in the borosilicate analogue) [14] and for this reason a more complex phase transition must occur.

3.3. Role of OSDA in ITQ-1 synthesis

The ITQ-1 samples synthesized here show different properties: the macroscopical aggregation and the primary particle thickness (related to a long-range crystalline order, as highlighted by XRD and SEM microscopy) and the amount of defective sites and the difference in angular distribution at the crystallographic sites (related to a short-range crystalline order, as depicted by spectroscopic methods). These features seem to be affected by both the composition of the synthesis gel and by the calcination procedure. The effect of the synthesis gel composition was examined by studying the organic fraction in the as-synthesized material and the presence of alkali cations in the framework. The effect of the calcination procedure resulting in the OSDA removal was
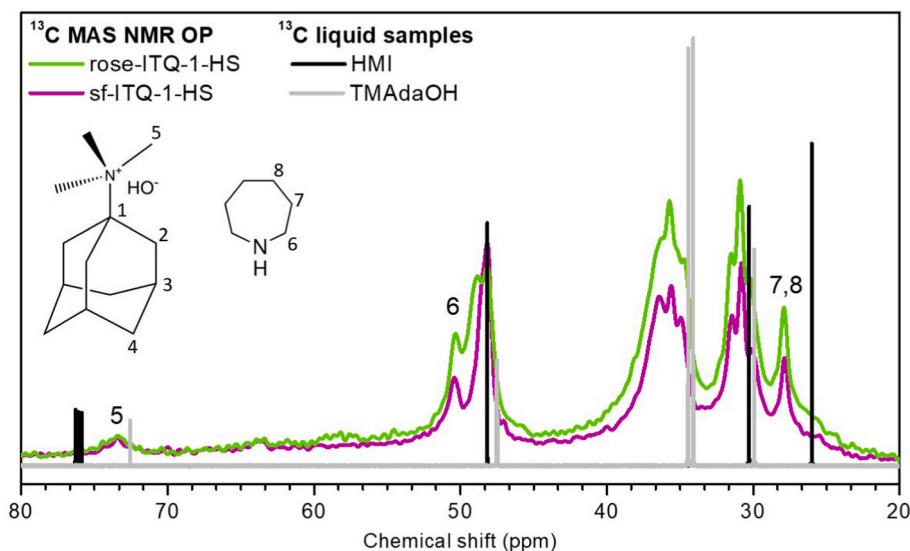
Fig. 5. ^{13}C OP-NMR spectra of as-synthesized rose-ITQ-1-HS and sf-ITQ-1-HS samples, compared with the liquid phase spectra of the pure OSDAs (HMI and TMAdaOH).

Table 4
C/N ratio, OSDAs per unit cell and OSDAs ratio for the rose-ITQ-1 and sf-ITQ-1 synthesis gels and for the as-synthesized samples determined by elemental analysis CHNS. 72 Si atoms are used to calculate the TMAda$^+$, HMI and H$_2$O molar ratio per unit cell in the synthesis gel composition.

	Synthesis gel		As-synthesized samples	
	rose-ITQ-1-HS	sf-ITQ-1-HS	rose-ITQ-1-HS	sf-ITQ-1-HS
C/N	8.80	9.13	9.91	9.92
TMAda$^+$/HMI	0.67	0.81	1.27	1.27
TMAda$^+$/unit cell	14.4	18.00	3.95	3.60
HMI/unit cell	21.6	22.32	3.11	2.83
TMAda$^+$/H$_2$O (*10^{-3})	6.67	5.68	–	–
HMI/H$_2$O (*10^{-3})	10.00	7.05	–	–
H$_2$O/SiO$_2$	30	44	–	–
Si/K	7.14	∞	1326	∞

examined by TG analysis and variable temperature IR experiments.

The ^{13}C OP-MAS-NMR spectra of the as-synthesized rose-ITQ-1-HS and sf-ITQ-1-HS samples are depicted in Fig. 5, compared with the liquid phase spectra of the two OSDA used (HMI and TMAdaOH). The signals in the ^{13}C OP-MAS-NMR spectra are affected by the type and amount of the organic molecules, by their location and by the possible interactions between them. The spectra contain similar signals, thus the different cavities in the two samples host the same organic molecule. If the same molecule would be placed in pores of different shape, its signals would be split or broadened. In MCM-22, HMI is reported to locate in both cavities and TMAda$^+$ is reported to be located only inside the supercages [25,45,46]. The main difference between the spectrum of rose-ITQ-1-HS and sf-ITQ-1-HS is the relative intensity of the signals. The absolute intensity is proportional to the absolute amount of organics in the zeolite, while the relative intensity is associated to the relative concentration of the two OSDAs. A complete assignment of the spectra is ventured due to the overlapping of chemical shifts [46,47]. The different absolute intensity suggests, however, that the amount of organic molecules is not the same in both samples. For this reason, CHNS elemental analysis was performed, and the results are summarized in Tables 4 and S10. The TMAda$^+$/HMI molar ratio is the same in both samples (Table 4), but the total amount of organics is higher in the rose-ITQ-1-HS than in the sf-ITQ-1-HS. Less OSDA molecules are incorporated in sample sf-ITQ-1-HS during the hydrothermal crystallization. The

reduced incorporation could be ascribed to the stronger gel dilution (lower HMI/H$_2$O and TMAda$^+$/H$_2$O ratios in Table 4). This may be the reason behind different stackings of the layers and the lower order along the *c* axis as shown by the sf-ITQ-1-HS, -calcA and -calcB samples. This is even more evident when the amount of TMAda$^+$ per unit cell is considered. Since TMAda$^+$ is the only OSDA placed in the internal supercages, it is the main directing agent responsible for the stacking. Considering that its theoretical amount should be 4 cations/unit cell [45], this number is perfectly respected in sample rose-ITQ-1-HS, while it is not the case for sf-ITQ-1-HS sample. A shortage of TMAda$^+$ cations will induce a more frequent layer mismatch, that generates more Si–OH defective groups at the junctions. The HMI/unit cell (in principle 3), as well, is in slight excess in the rose-ITQ-1-HS sample. The lower amount of HMI in the sf-ITQ-1-HS sample makes impossible to supply for the lack of TMAda$^+$ and probably induces the formation of additional Si–OH groups, justifying the higher amount of silanol nests visible in the transmission IR spectra of sf-ITQ-1-calcA and sf-ITQ-1-calcB samples. Despite the lack of OSDA molecules, sample sf-ITQ-1-HS crystallized in the excess of H$_2$O molecules, that acts as space filler.

Furthermore, the higher OH/Si ratio in sf-ITQ-1 in respect to that one of rose-ITQ-1 may influence the surface charge of the layers. This could obstacle the correct stacking and consequently the TMAda$^+$ incorporation.

The lower defectivity exhibited for rose-ITQ-1-calcA and -calcB samples compared to samples sf-ITQ-1-calcA and -calcB could also be influenced by the presence of K$^+$ cations, coming from the K$_2$CO$_3$ used for the preparation of the precursor gels, sometimes acting as inorganic SDA. However, no K$^+$ was detected by chemical analysis, since it is not retained in the structure and its residual amount in the structure is negligible (Tables 4 and S11).

The transmission IR spectra (Fig. S13) showed that the defectivity of the calcined samples was also slightly affected by the calcination procedure, the gel composition being equal, as highlighted by the behavior of band assigned to Si–OH nests in the different samples. The calcination procedure was further followed by TG and variable temperature transmission IR spectroscopy, adopting the same calcination procedures (*procedure A* and *procedure B*). The TG curves (Fig. 6) show weight losses tentatively explained by using the DTG curves and the IR experiments. The species expected to degrade/leave the sample during the calcination are the HMI, the TMAda$^+$ and the H$_2$O produced upon condensation of the Si–OH groups. The OSDAs degradation occurs in the same way, when the same calcination procedure was used, regardless of the
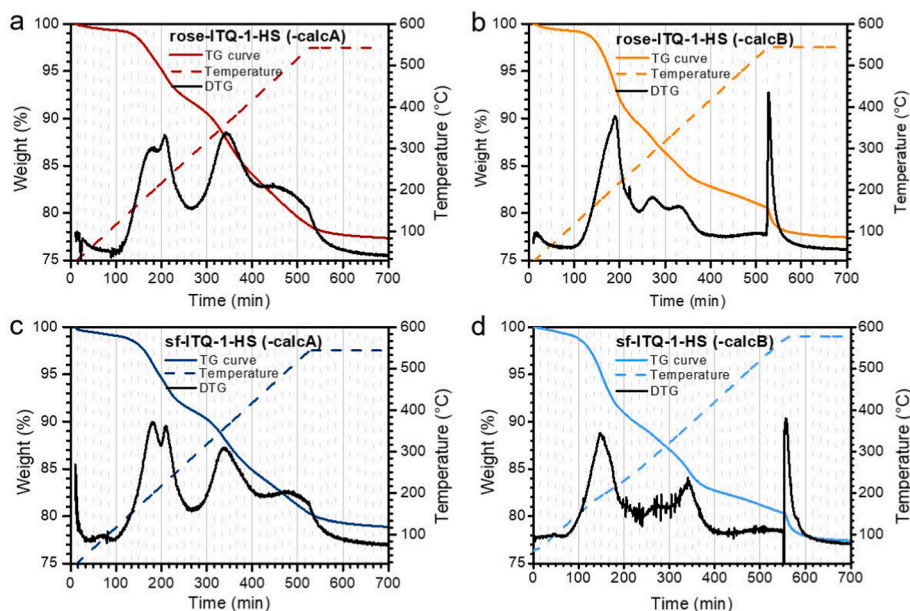
Fig. 6. TG analyses of rose-ITQ-1-HS sample calcined with *procedure A* (a), rose-ITQ-1-HS sample calcined with *procedure B* (b), sf-ITQ-1-HS sample calcined with *procedure A* (c) and sf-ITQ-1-HS sample calcined with *procedure B* (d). *Procedure A*: 1 °C/min up to 550 °C under dry air, followed by 3 h in isothermal conditions under the same flux. *Procedure B*: 1 °C/min up to 580 °C under N_2 flux, followed by 3 h in isothermal conditions under dry air.

synthesis gel composition (rose-ITQ-1-HS or sf-ITQ-1-HS). The DTG curves of the samples calcined with *procedure A* (Fig. 6a,c) present four peaks, suggesting that the degradation of the organic molecules proceed by several steps. The DTG curves of those calcined with *procedure B* (Fig. 6b,d) show instead three broad signals and one very sharp peak, which is due to the sudden oxidation of any organic residuals occurring by switching from N_2 to air flow. A moderately sharp peak is visible at around 200 °C in the DTG of all the samples, and it is probably due to the H_2O loss. The results are consistent with the previous reports on phase transition between separated single layers and calcined zeolite phases [14]. The combination of the elemental CHNS analysis data with the TG

analysis allows also justifying the exceptionally high amount of Si–OH groups visible in the ^{29}Si OP-MAS-NMR spectra of the as-synthesized samples (Fig. 4c). The amount of H_2O produced upon calcination, determined by difference between the quantification with TG and with CHNS analysis, was coherent with the equivalent number of H_2O molecules generated during the condensation of the amount of Si–OH groups before the calcination as determined by the ^{29}Si OP-NMR spectra shown in Fig. 4c. This means that, even if a simple condensation of the layers is unlikely to occur as explained earlier by the deconvolution of the ^{29}Si NMR spectra, we saw that an exceptionally high amount of Si–OH groups in the as-synthesized material ($\approx$22 %) undergoes
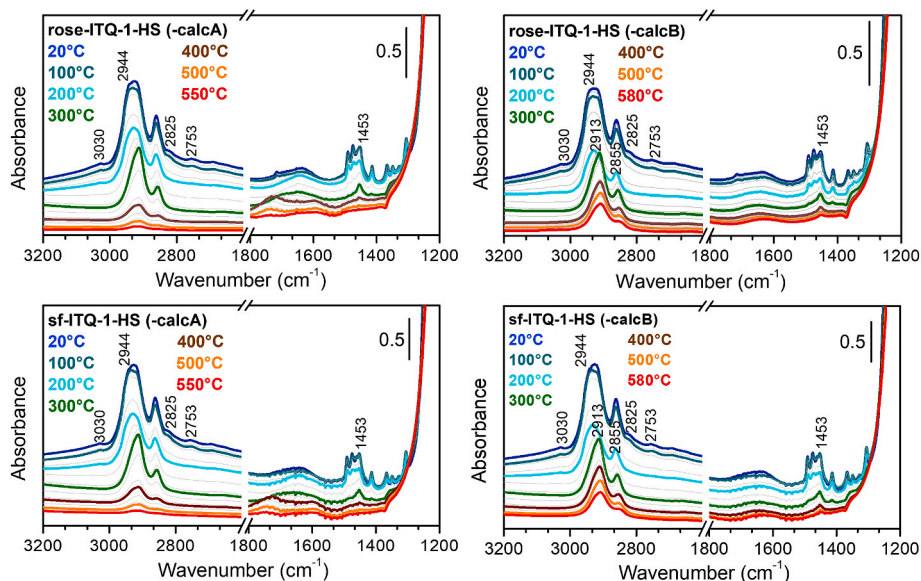

Fig. 7. Transmission IR spectra of rose-ITQ-1-HS sample calcined with *procedure A* (a), rose-ITQ-1-HS sample calcined with *procedure B* (b), sf-ITQ-1-HS sample calcined with *procedure A* (c) and sf-ITQ-1-HS sample calcined with *procedure B* (d). The grey spectra shown are recorded every 20 min. The colored spectra correspond to the temperatures: 20 °C blue, 100 °C dark cyan, 200 °C light cyan, 300 °C green, 400 °C brown, 500 °C orange and 550 °C (a and c panels) or 580 °C (c and d panels) red. *Procedure A*: 1 °C/min up to 550 °C under 20 vol% O_2 in Ar, followed by 3 h in isothermal conditions under the same flux. *Procedure B*: 1 °C/min up to 580 °C under pure Ar flux, followed by 3 h in isothermal conditions under 20 vol% O_2 in Ar.

condensation during the phase transition between the 2D precursor to the 3D calcined zeolite. Details about the determination of the H_2O molecules loss are reported in section 2.3.1 of the ESI.

The identification of several degradation steps of the OSDA molecules were further explored by simulating the calcination procedure and recording the IR spectra during the heating ramps and at 550 °C and 580 °C. Fig. 7 shows the spectra recorded during the heating ramp of the two as-synthesized samples (rose-ITQ-1-HS and sf-ITQ-1-HS), calcined with the two procedures (-calcA or -calcB), reported in the 3200-1200 cm^{-1} spectral range. The full spectra are presented in Fig. S17. The signals of the OSDA molecules are localized in the 3050-2800 cm^{-1} and 1550-1250 cm^{-1} regions. The 3050-2800 cm^{-1} region hosts the C–H stretching mode bands, while the C–H bending and deformation mode bands fall in the 1500-1250 cm^{-1} region. The degradation pathway of the OSDA molecules revealed by diminishing of the IR bands intensity upon the temperature increase. As observed in the TG plots (Fig. 6), the degradation path is only affected by the calcination procedure (*A* or *B*) and not by the synthesis gel composition (the bands decrease in the same way and at the same temperature in panels a–c and b-d, corresponding to the *procedures A* and *B*, respectively). Below 300 °C, the degradation occurs similarly by heating in an oxidant or inert atmosphere. Upon increasing the temperature from 30 °C to 300 °C (see blue, dark cyan, light cyan and green spectra in Fig. 7), the thermal degradation of tri-methylamine (TMA) is observed (signals at 3050, 2825 and 2753 cm^{-1}). The TMA is a fragment of the $TMAda^+$ OSDA. The fragmentation of $TMAda^+$ to give TMA and adamantane group (Ada) can occur during the calcination or already during the hydrothermal treatment. The vibrational bands present in the spectra recorded at 30 °C, before starting the calcination (blue spectra in Fig. 7), suggest that the two scenarios are both possible. The bands at 2825 and 2753 cm^{-1} are assigned to the symmetric stretching of CH_3 groups ($\nu_{sym}(CH_3)$) of TMA, meaning that the TMA is already present before the calcination and hence it is partially formed during the hydrothermal treatment. The band at 3030 cm^{-1} is associated to the asymmetric stretching of CH_3 groups ($\nu_{asym}(CH_3)$) in trimethylammonium cations, testifying that $TMAda^+$ is still present in the as-synthesized sample. At 300 °C, the degradation of TMA is completed (note the disappearance of the signals at 3030, 2825, 2753 cm^{-1} in the green spectra). Around 200 °C, the degradation of HMI starts (light cyan spectra) and at 400 °C it is almost finished (brown spectra), as shown by the complete disappearance of the signals at 1453 and 2944 cm^{-1} assigned to a deformation of the CH_2 groups next to the N in HMI ($\delta(CH_2)$) and to the asymmetric stretching of CH_2 ($\nu_{asym}(CH_2)$) and of the signals between 1570 and 1300 cm^{-1} (deformations of the CH_2 group in aliphatic chains). Above 300 °C the degradation pathway deviates depending on the procedure (*A* or *B*). Here the oxidation or the thermal degradation of the Ada fraction of $TMAda^+$ starts. The Ada removal can be followed observing the CH stretching region of the spectra, where signals at 2913 and 2855 cm^{-1} are preserved, and the CH_2 deformation range (band at 1455 cm^{-1}) that is barely visible after the complete elimination of the TMA and of the HMI. When an oxidant atmosphere is used (*procedure A*, shown in Fig. 7a and c) the bands assigned to the Ada group almost completely disappear at the end of the heating ramp (red spectrum). In contrast, in the presence of an inert atmosphere, a significant quantity of Ada is preserved till the end of the heating ramp, at a higher temperature that its sublimation point (109–112 °C), as shown by the presence of both stretching and bending modes of Ada in the red spectra (Fig. 7b,d). In this case Ada is probably trapped into the internal super-cages of the framework, due to its large size (6.8 x 7.6 × 7.4 Å) [48], bigger than the 10 MR apertures. It is, however, immediately burned when O_2 was sent in the flow, (see the lower plots of Figs. S16b and d). This is confirmed by the mass spectrometry analyses of the gas phase downstream to the IR spectrophotometer (Fig. S17). The IR experiments allow disclosing the reason of the slight lower amount of silanol nests in rose-ITQ-1-calcB and sf-ITQ-1-calcB samples compared to rose-ITQ-1-calcA and sf-ITQ-1-calcA materials, respectively. When the *procedure B* is used, a fraction of the OSDAs (the Ada group) is preserved at high temperature, and it is immediately burned by sending O_2 in the flow. The presence of the OSDA at high temperature probably helps healing the defects, determining the lower amount of silanols nests in rose-ITQ-1-calcB and sf-ITQ-1-calcB.

4. Conclusions

In this work, four siliceous zeolitic samples with MWW framework were prepared using different compositions of the precursor synthesis gel and calcination procedures. The XRD and SEM results revealed that the samples differ in particle thickness and crystalline order along the *c* axis. The two properties are related, since when the MWW single layers are stacked in a partially disordered way, the growth along the *c* axis is hindered, because of the more frequent interruption of the crystalline order. The different degree of short crystalline ordering is also observed by IR, Raman and ^{29}Si NMR spectroscopies. The combination of TGA, elemental analysis (CHNS) and ^{13}C NMR spectroscopy allow understanding that the amount of OSDA incorporated in the crystalline sample is higher when the synthesis gel is more concentrated (higher OSDA/H_2O molar ratio), and that this condition is necessary for obtaining the ITQ-1 material with perfectly stacked layers. In particular, the $TMAda^+$, located in the internal super-cages, is responsible for the correct stacking of the layers, while the HMI, located in the sinusoidal channels, is responsible for the formation of individual layers during the hydrothermal treatment [8,22,25]. In the sf-ITQ-1 sample, both the OSDA are in stoichiometric defect, but this is counterbalanced by an excess of H_2O that is acting as space filler. The lack of OSDAs also resulted in the formation of high amount of silanol sites present in the sf-ITQ-1 samples. The zeolites with low order along the *c* axis are more defective, and the defects are probably located at the points where the mismatch between the layers occurs. The defectivity was also proved to be slightly affected by the calcination procedure: indeed, by calcining the sample under inert atmosphere, a fraction of the OSDA was preserved inside the framework even at high temperature and suddenly burned by contact with pure O_2. A slightly lower defectivity of the samples calcined by heating under inert atmosphere was observed instead. Finally, these samples were shown to spontaneously aggregate into hollow macro-spheres and that the way of aggregation is probably regulated by the gel dilution and by the ratio between the two used OSDAs. This property must surely be further investigated due to the boost that macro-voids can give to diffusivity properties.

CRediT authorship contribution statement

Francesca Rosso: Writing – original draft, Visualization, Validation, Methodology, Investigation, Formal analysis, Conceptualization. **Alessia Airi:** Writing – review & editing, Supervision, Investigation, Conceptualization. **Matteo Signorile:** Writing – review & editing, Supervision, Conceptualization. **Eddy Dib:** Writing – review & editing, Validation, Supervision, Methodology, Investigation, Formal analysis, Conceptualization. **Silvia Bordiga:** Writing – review & editing, Resources, Funding acquisition, Conceptualization. **Valentina Crocellà:** Writing – review & editing, Supervision, Conceptualization. **Svetlana Mintova:** Writing – review & editing, Supervision, Conceptualization. **Francesca Bonino:** Writing – review & editing, Supervision, Resources, Project administration, Funding acquisition, Conceptualization.

Declaration of competing interest

The authors declare that they have no known competing financial interests or personal relationships that could have appeared to influence the work reported in this paper.

Data availability

Data will be made available on request.

Acknowledgements

Appendix A. Supplementary data

Supplementary data to this article can be found online at https://doi.org/10.1016/j.micromeso.2023.112924.

References

[1] W.J. Roth, P. Nachtigall, R.E. Morris, J. Čejka, Chem. Rev. 114 (2014) 4807–4837.
[2] J. Přech, P. Pizarro, D.P. Serrano, J. Cejka, Chem. Soc. Rev. 47 (2018) 8263–8306.
[3] U. Díaz, A. Corma, Dalton Trans. 43 (2014) 10292–10316.
[4] C. Baerlocher, L.B. McCusker, Database of Zeolite Structures, 1978.
[5] C. Baerlocher, L.B. McCusker, Database of Zeolite Structures, 1997.
[6] C. Baerlocher, L. McCusker, Database of Zeolite Structures, 1978.
[7] M. Choi, K. Na, J. Kim, Y. Sakamoto, O. Terasaki, R. Ryoo, Nature 461 (2009) 246–249.
[8] A. Corma, C. Corell, J. Pérez-Pariente, Zeolites 15 (1995) 2–8.
[9] M.E. Leonowicz, J.A. Lawton, S.L. Lawton, M.K. Rubin, 1979, Science 264 (1994) 1910–1913.
[10] M.K. Rubin, P. Chu, Composition of synthetic porous crystalline material, its synthesis and use, Science 325 (4) (1990) 954.
[11] S.I. Zones, Microporous Mesoporous Mater. 144 (2011) 1–8.
[12] T.F. Degnan, C.M. Smith, C.R. Venkat, Appl. Catal. Gen. (2001) 283–284.
[13] M. Položij, H.V. Thang, M. Rubeš, P. Eliášová, J. Čejka, P. Nachtigall, Dalton Trans. 43 (2014) 10443–10450.
[14] R. Millini, G. Perego, W.O. Parker, G. Bellussi, L. Carluccio, Microporous Mater. 4 (1995) 221–230.
[15] H.K. Beyer, H.G. Karge, I. Kiricsi, J.B. Nagy, W.J. Roth, C.T. Kresge, J.C. Vartuli, M. E. Leonowicz', A.S. Fung, S.B. Mccullen, Stud. Surf. Sci. Catal. (1995) 301–308.
[16] A. Corma, V. Fornés, J.M. Guil, S. Pergher, T.L.M. Maesen, J.G. Buglass, Microporous Mesoporous Mater. 38 (2000) 301–309.
[17] S.L. Lawton, A.S. Fung, G.J. Kennedy, L.B. Alemany, C.D. Chang, G.H. Hatzikos, D. N. Lissy, M.K. Rubin, H.K.C. Timken, S. Steuernagel, D.E. Woessner, J. Phys. Chem. 100 (1996) 3788–3798.
[18] A.S. Fung, S.L. Lawton, J. Roth, Wieslaw, Synthetic layered MCM-56, its synthesis and use, US 5,362,697 (1994).
[19] B. Gil, W.J. Roth, W. Makowski, B. Marszalek, D. Majda, Z. Olejniczak, P. Michorczyk, Catal. Today 243 (2015) 39–45.
[20] G.G. Juttu, R.F. Lobo, Microporous Mesoporous Mater. 40 (2000) 9–23.
[21] P. Wu, T. Tatsumi, T. Komatsu, T. Yashimay, J. Catal. 202 (2001) 245–255.
[22] H. Xu, Y. Guan, X. Lu, J. Yin, X. Li, D. Zhou, P. Wu, ACS Catal. 10 (2020) 4813–4819.
[23] T. Wan, F. Jin, X. Cheng, J. Gong, C. Wang, G. Wu, A. Liu, Appl. Catal. Gen. 637 (2022) 118542–118554.
[24] P.M. Piccione, C. Laberty, S. Yang, M.A. Camblor, A. Navrotsky, M.E. Davis, J. Phys. Chem. B 104 (2000) 10001–10011.
[25] M.A. Camblor, A. Corma, M.J. Díaz-Cabañas, C. Baerlocher, J. Phys. Chem. B 102 (1998) 44–51.
[26] M. Thommes, K. Kaneko, A.V. Neimark, J.P. Olivier, F. Rodriguez-Reinoso, J. Rouquerol, K.S.W. Sing, Pure Appl. Chem. 87 (2015) 1051–1069.
[27] Micromeritics Instrument Corporation, 2012.
[28] D.M. Dawson, R.F. Moran, S.E. Ashbrook, J. Phys. Chem. C 121 (2017) 15198–15210.
[29] C. Baerlocher, L.B. McCurker, Database of Zeolite Structures, 2016.
[30] M. Fabbiani, A. Morsli, G. Confalonieri, T. Cacciaguerra, F. Fajula, J. Haines, A. Bengueddach, R. Arletti, F. Di Renzo, Microporous Mesoporous Mater. 332 (2022) 111678–111685.
[31] N. Chu, J. Wang, Y. Zhang, J. Yang, J. Lu, D. Yin, Chem. Mater. 22 (2010) 2757–2763.
[32] A. Schwanke, J. Villarroel-Rocha, K. Sapag, U. Díaz, A. Corma, S. Pergher, ACS Omega 3 (2018) 6217–6223.
[33] S. Cao, Y. Shang, Y. Liu, J. Wang, Y. Sun, Y. Gong, G. Mo, Z. Li, P. Liu, Microporous Mesoporous Mater. 315 (2021) 110910–110921.
[34] M. Król, W. Mozgawa, W. Jastrzbski, K. Barczyk, Microporous Mesoporous Mater. 156 (2012) 181–188.
[35] D. Scarano, A. Zecchina, S. Bordiga, F. Geobaldo, G. Spoto, G. Petrini, G. Leofanti, M. Padovan, G. Tozzola, J. Chem. Soc., Faraday Trans. 89 (1993) 4123–4130.
[36] K. Ogorzały, B. Gil, B. Mazur, W. Makowski, W.J. Roth, Microporous Mesoporous Mater. 324 (2021) 111300–111307.
[37] B. Gil, W. Makowski, B. Marszalek, W.J. Roth, M. Kubu, J. Čejka, Z. Olejniczak, J. Chem. Soc. Dalton Trans. 43 (2014) 10501–10511.
[38] W. Mozgawa, W. Jastrzębski, M. Handke, J. Mol. Struct. (2005) 663–670.
[39] Y. Y. Xiong, C. Li, F.-S. Xiao, Microporous Mesoporous Mater. 46 (2001) 23–34.
[40] F. Fengtao, F. Zhaochi, L. Can, Chem. Soc. Rev. 39 (2010) 4794–4801.
[41] M. Signorile, V. Crocellà, A. Damin, B. Rossi, C. Lamberti, F. Bonino, S. Bordiga, J. Phys. Chem. C 122 (2018) 9021–9034.
[42] S. Bordiga, I. Roggero, P. Ugliengo, A. Zecchina, V. Bolis, G. Artioli, R. Buzzoni, G. Marra, F. Rivetti, G. Spano, C. Lamberti, J. Chem. Soc. Dalton Trans. (2000) 3921–3929.
[43] S. Bordiga, P. Ugliengo, A. Damin, C. Lamberti, G. Spoto, A. Zecchina, G. Spanò, R. Buzzoni, L. Dalloro, F. Rivetti, Top. Catal. 15 (2001) 43–52.
[44] F. Pascale, P. Ugliengo, B. Civalleri, R. Orlando, P. D'Arco, R. Dovesi, J. Chem. Phys. 117 (2002) 5337–5346.
[45] S.L. Njo, H. Van Konigsveld, B. Van De Graaf, C. Barelocher, L.B. Mccusker, in: M. M.J. Treacy, B.K. Marcus, M.E. Bisher, J.B. Higgins (Eds.), 12th International Zeolite Conference, 1999, pp. 2519–2524.
[46] P. Lu, L. Gómez-Hortigüela, M.A. Camblor, Chem. Eur J. 25 (2019) 1561–1572.
[47] S. Sabnis, V.A. Tanna, J. Gulbinski, J. Zhu, S.S. Nonnenmann, G. Sheng, Z. Lai, H. H. Winter, W. Fan, Microporous Mesoporous Mater. 315 (2021) 110883–110890.
[48] F. Jiménez-Cruz, J.L. García-Gutiérrez, Arab. J. Chem. 13 (2020) 8592–8599.